WILEY-VCH

DOI: 10.1002/ ente.201801121R1
Article type: Full Paper

Synergistic effects of Mo_2C-NC@Fe_xCo_y core-shell nanoparticles in electrocatalytic overall water splitting reaction

*Shiping Wang, Georg Bendt, Sascha Saddeler, and Stephan Schulz**

Faculty of Chemistry and Center for NanoIntegration (CENIDE), University of Duisburg-Essen, Essen 45117, Germany
E-mail: stephan.schulz@uni-due.de

Keywords: bi-functional electrocatalysts, core-shell nanoparticles, N-doped graphene, transition metals, water splitting reaction

Transition metals (TMs) are highly investigated as nonprecious electrocatalysts for hydrogen evolution (HER) and oxygen evolution (OER) reactions, there is a strong demand for highly efficient and inexpensive catalysts for overall water splitting. Herein, the bimetallic Co_xFe_y alloy nanoparticles encapsulated in an N-doped graphene shell containing molybdenum carbide (Mo_2C) nanoparticles are synthesized by the pyrolysis of cobalt ferrite $Co_xFe_{3-x}O_4$ nanoparticles coated by molybdic acid-cross-linked melamine-formaldehyde (MF) resin. Molybdic acid not only serves as precursor for the formation of highly dispersed Mo_2C nanoparticles in the N-doped graphene shell but also enhances the thermal stability of the organic shell, resulting in the formation of smaller Co_xFe_y cores. The formation of Mo_2C nanoparticles in the graphene shell is promoted by the cobalt ferrite core. Interestingly, the synergistic presence of Mo_2C nanoparticles not only enhances the HER activity of the material, but also renders a partial breakage of the graphene shell which increases the surface concentration of OER active Co and therefore enhances the OER activity. The as-prepared TMs-based materials serve as bi-functional catalysts for the overall water splitting and exhibit improved electrocatalytic performances compared to standard cells based on precious metals, with potentials of 1.53 V and 1.60 V at 10 mA cm^{-2} and 20 mA cm^{-2} in alkaline media, respectively.

1. Introduction

The massive consumption of unsustainable fossil fuels is largely to blame for the energy crisis and current environmental problems that our planet is facing today, thus the investigation of renewable energy systems such as water splitting, fuel cells, and metal-air batteries, is crucial for the development of sustainable energy technologies in the near future.[1] Electrochemical water splitting reactions ($H_2O \rightarrow H_2 + ½O_2$) for instance use electrical energy to generate clean H_2 and O_2 gases from sustainable water sources.[2] Unfortunately, the key half reactions of water splitting systems, which include the oxygen evolution reaction (OER) and the hydrogen evolution reaction (HER), generally require high overpotential and involve a substantial amount of energy consumption due to the sluggish reaction kinetics of these processes.[3] To promote the overall efficiency of water splitting reactions, extensive research was focused on the development of highly active electrocatalysts, which typically contain noble metals such as Pt, Ru, and Ir.[4] However, due to their high cost and limited chemical and thermal stabilities, these types of catalysts are inconvenient for large scale technical applications. Consequently, the design of inexpensive and highly efficient electrocatalysts for overall water splitting processes is essential for the societal pursuit of renewable energy.

Among the many promising nonprecious electrocatalysts, materials containing 3d transition-metals (3d-TM) [5] such as Fe, Co, and Ni have attracted particular attention due to their earth-abundant sources and favorable cost.[6] For instance, Co-containing electrocatalysts have been developed due to their relatively low OER overpotentials in alkaline media.[6b, 6d, 7] Interestingly, the surface of the Co-based electrocatalysts in alkaline OER is oxidized to a thermodynamically stable Co-(oxy)hydroxide (CoOOH), which serves as the active species in OER.[8] Unfortunately, the electrochemical performance of sole 3d TMs, alloys, oxides, and hydroxides is often limited by a self-aggregation behavior observed during long-term

electrochemical processes.[9] Supporting these electrocatalysts on stable and conductive substrates such as porous carbon or graphene yields composite materials with dispersed active sites, which exhibited enhanced electron transport capacities and showed improved catalytic activity.[10] In addition, encapsulating the active metal in a thin graphene layer was found to inhibit aggregation and oxidation processes.[6c, 10b, 11] However, the reduced active site density on the surface and poor electron penetration from the metal-based core to the carbon surface due to the encapsulation method have instead hampered the overall electrocatalytic activity of these composite materials.

Very recently, core-shell nanoparticles consisting of 3d TMs such as Co and Ni encapsulated in a graphene layer containing chemically coupled molybdenum carbide nanoparticles, including γ-MoC and Mo_2C, were found to show promising electrocatalytic performances.[12] Due to their high chemical stability, high electrical conductivity, and comparable d-band structure in comparison with precious metals, Mo carbides have been intensively studied as electrocatalysts for HER.[13] These materials are typically produced at high calcination temperatures using a sintering process, by which they often form large aggregates.[13a-b] To some extent, the coalescence of the Mo carbide particles can be reduced by coupling them to the graphene layer, whose formation is catalyzed by Co or Ni compounds.[12] As-formed core-shell particles showed improved catalytic performances in HER and OER processes, owing to the beneficial effect of an easier electron transfer from Co or Ni to the contacted Mo carbides.[12b-e] In addition, the overall electronic properties of the composite materials can be further tuned by nitrogen doping, resulting in an enhanced catalytic activity.[6a, 7b, 10b, 14] Surprisingly, despite the promising electrocatalytic properties of Fe-based materials and the favorable effects of Fe-based materials on the formation of Mo carbides, only a few reports on materials containing Mo carbides coupled to Fe-catalyzed graphene layers are known.[6a, 11c, 15] The synthesis of such composite materials with highly dispersed active sites on the nanoparticle surface is a challenging task since the active

components tend to coalesce with subsequent formation of largely agglomerated particles. In this case, the material synthesis must address the structural stabilization of the catalytically active sites to avoid the agglomeration of the particles and therefore improve their catalytic performance in electrocatalytic applications such as the water splitting reaction.

We herein report on the synthesis of Co_xFe_y alloy nanoparticles encapsulated in N-doped graphene shell containing additional Mo carbide nanoparticles. In contrast to typically applied evaporation and solid grinding methods,[12e, 12f, 15a] the composite (core-shell) material was prepared by pyrolysis of cobalt ferrite $Co_xFe_{3-x}O_4$ NPs encapsulated in MF resin cross-linked by molybdic acid. This specific precursor was obtained by compositing the cobalt ferrite $Co_xFe_{3-x}O_4$ nanoparticle with molybdic acid and melamine-formaldehyde (MF) resin under hydrothermal reaction. Calcination of this precursor at a relatively low temperature of 600 °C promotes the formation of a Co_xFe_y alloy core encapsulated in a N-doped graphene shell (NC) containing small Mo_2C nanoparticles (Mo_2C-NC@Co_xFe_y). The effect of Fe, Co, and Mo sources on the textural structure and properties of the Mo_2C-NC@Co_xFe_y material was analyzed. Furthermore, as bi-functional electrocatalysts in HER and OER reactions of the overall water splitting, the electrocatalytic performance of the resulting Mo_2C-NC@Co_xFe_y materials were closely investigated.

2. Results and Discussion

2.1. Material synthesis and characterization: The composite material consisting of a Co_xFe_y alloy core encapsulated in an N-doped graphene shell (NC) containing small Mo_2C nanoparticles (Mo_2C-NC@Co_xFe_y) was synthesized by calcination of the corresponding precursors at 600 °C in Ar flow (Scheme 1).

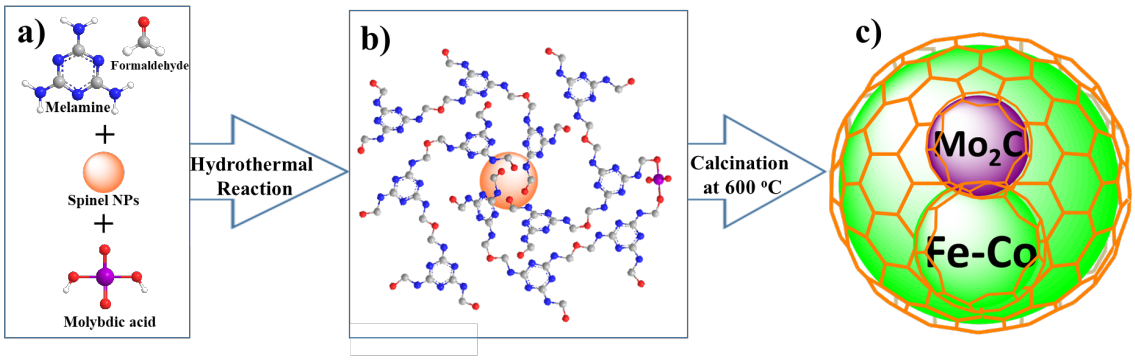

Scheme 1. Schematic illustration of the preparation process for b) the precursor and c) the calcined composite material (Mo_2C-NC@CoFe).

The reaction parameters for these as-prepared samples are given in Table S1, and sample 5 was exemplarily studied in detail. The precursor material was characterized by XRD (Figure S1) and FT-IR spectroscopy (Figure S2), confirming the spinel structure of the cobalt ferrite nanoparticles and the presence of the amorphous molybdic acid cross-linked MF resin. Transmission electron microscopy (TEM) images and EDX elemental maps further proved the formation of 5 nm-sized CoFe spinel nanoparticles coated by an amorphous organic carbon shell (Figure S3), which contains homogeneously distributed Mo atoms. XRD patterns (Figure 1a) of the material (sample 5) after calcination confirmed the presence of CoFe alloy and Mo_2C nanoparticles, and the mean size of their crystalline domains (CoFe 19 nm, Mo_2C 6 nm) were calculated according to the Debye Scherrer equation. Raman spectroscopy (Figure S4A) clearly proved the presence of graphitic carbon with an I_D/I_G value of 0.98. TEM studies revealed the formation of nanoparticles with an average size of about 18 nm (Figure 1b, Figure S5B), which closely agrees with the size of crystalline domains of the XRD results.

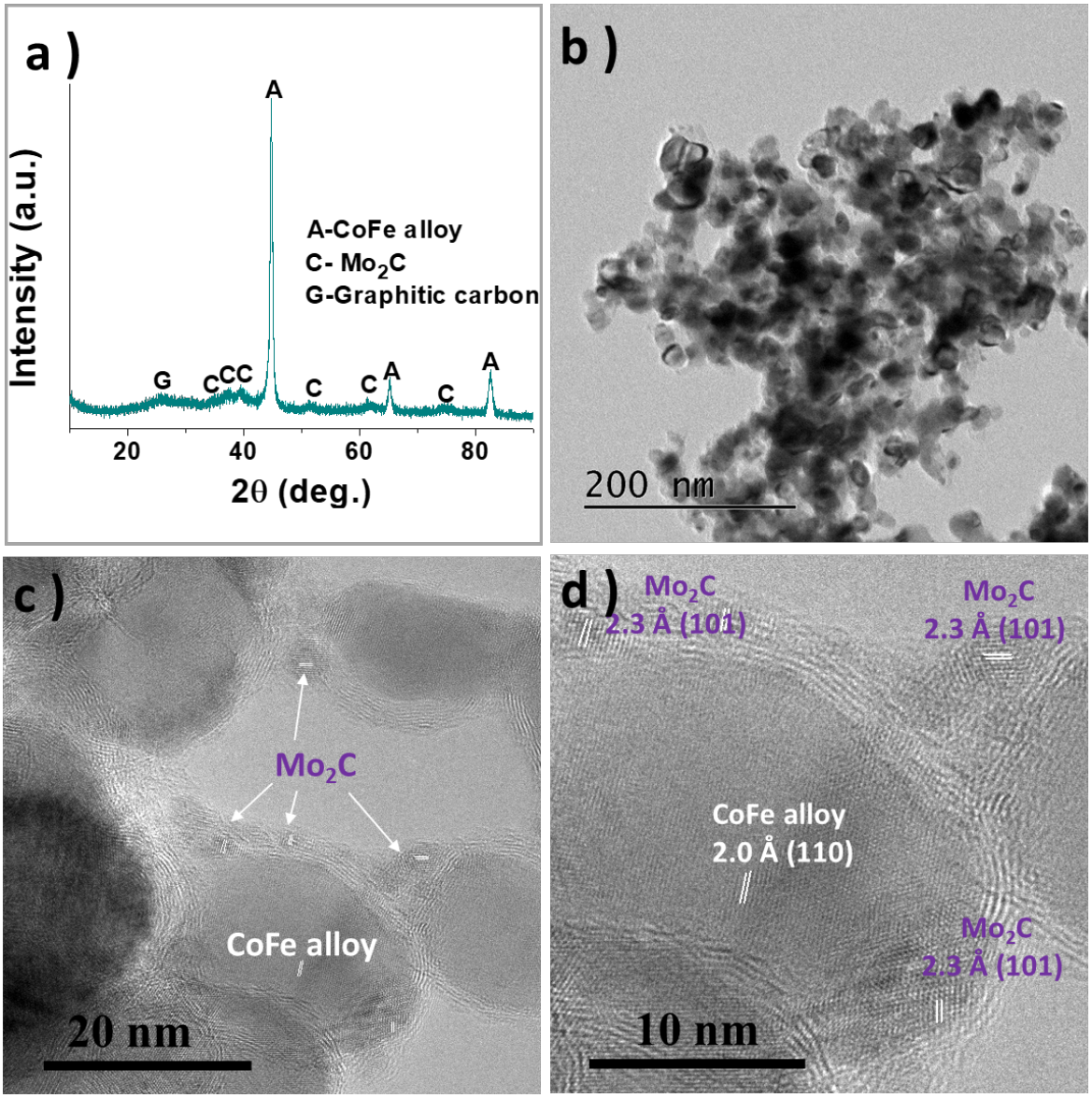

Figure 1. X-ray diffractogram (a) and (HR) TEM images (b, c, d) of Mo_2C-NC@CoFe composite (sample 5) as-formed upon pyrolysis of the corresponding precursor material at 600 °C.

High-resolution transmission electron microscopy (HR-TEM) images (Figures 1c, 1d) and EDX elemental maps of different elements (Figure 2) proved that the CoFe alloy nanoparticles are encapsulated in the N-doped graphene shell, which contains tiny Mo_2C nanoparticles that are preferentially incorporated and dispersed in the graphene shell. This form of structural stabilization hampers unwanted (surface) molybdenum oxidation and may therefore lead to a favorable electrocatalytic performance.

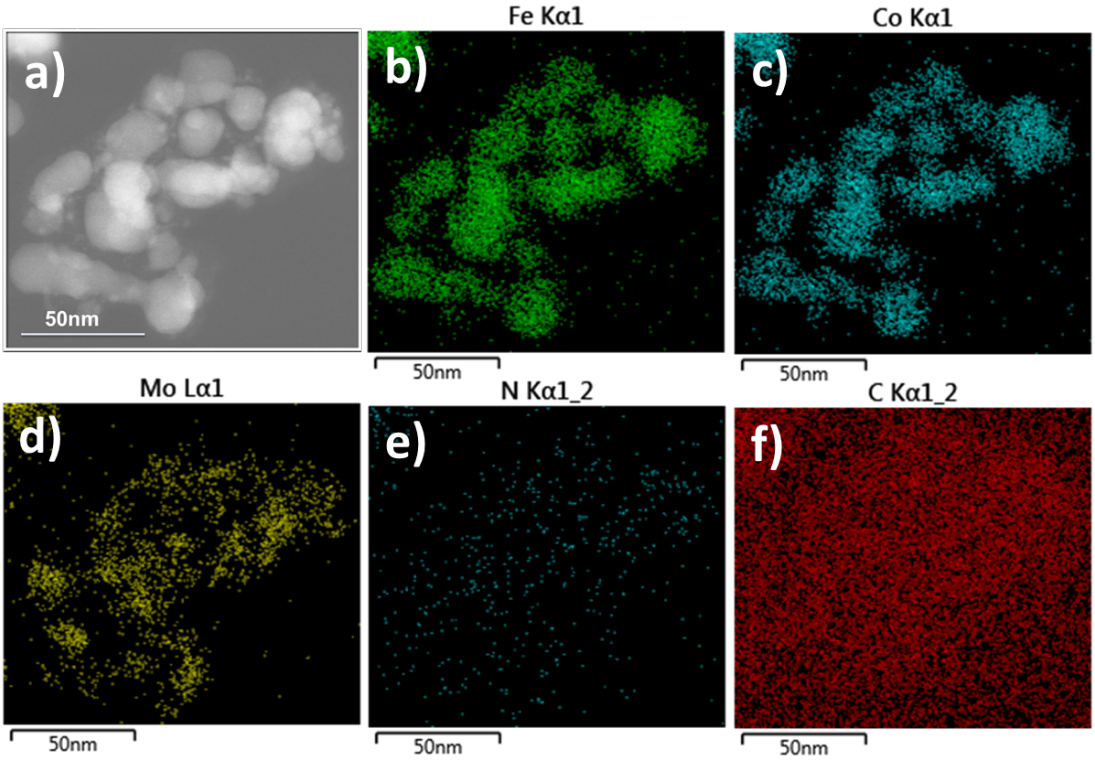

Figure 2. a) HAADF-STEM image of Mo_2C-CN@CoFe composite (sample 5) as-formed upon thermolysis of the corresponding precursor material at 600 °C and the corresponding EDX elemental maps for b) Fe, c) Co, d) Mo, e) N and f) C.

X-ray photoelectron spectroscopy (XPS) proved the existence of C, N, O, Fe, Co, and Mo in the composite material (Figure 3a). The bulk and surface compositions of different samples are given in Tables S2 and S5. The observed molar ratios of the metals as-determined by atomic absorption spectroscopy (AAS) correlate very well with the amount of metal sources used for the synthesis of the precursor materials. In addition, the C content of the bulk materials as determined by elemental analysis was generally lower than the surface carbon concentration as determined by XPS (Tables S2, S5), whereas the surface concentrations of Co and Fe are generally far below the values obtained by AAS for the bulk materials (i.e. sample 5: Co 5.67 wt%, Fe 5.45 wt% vs. Co 30.04 wt%, Fe 28.16 wt%). According to ultraviolet visible absorption spectroscopy (UV-vis), the Mo concentration of sample 5 is about 18.25 wt%, which is slightly less than the Mo concentration (24.70%) determined by XPS.

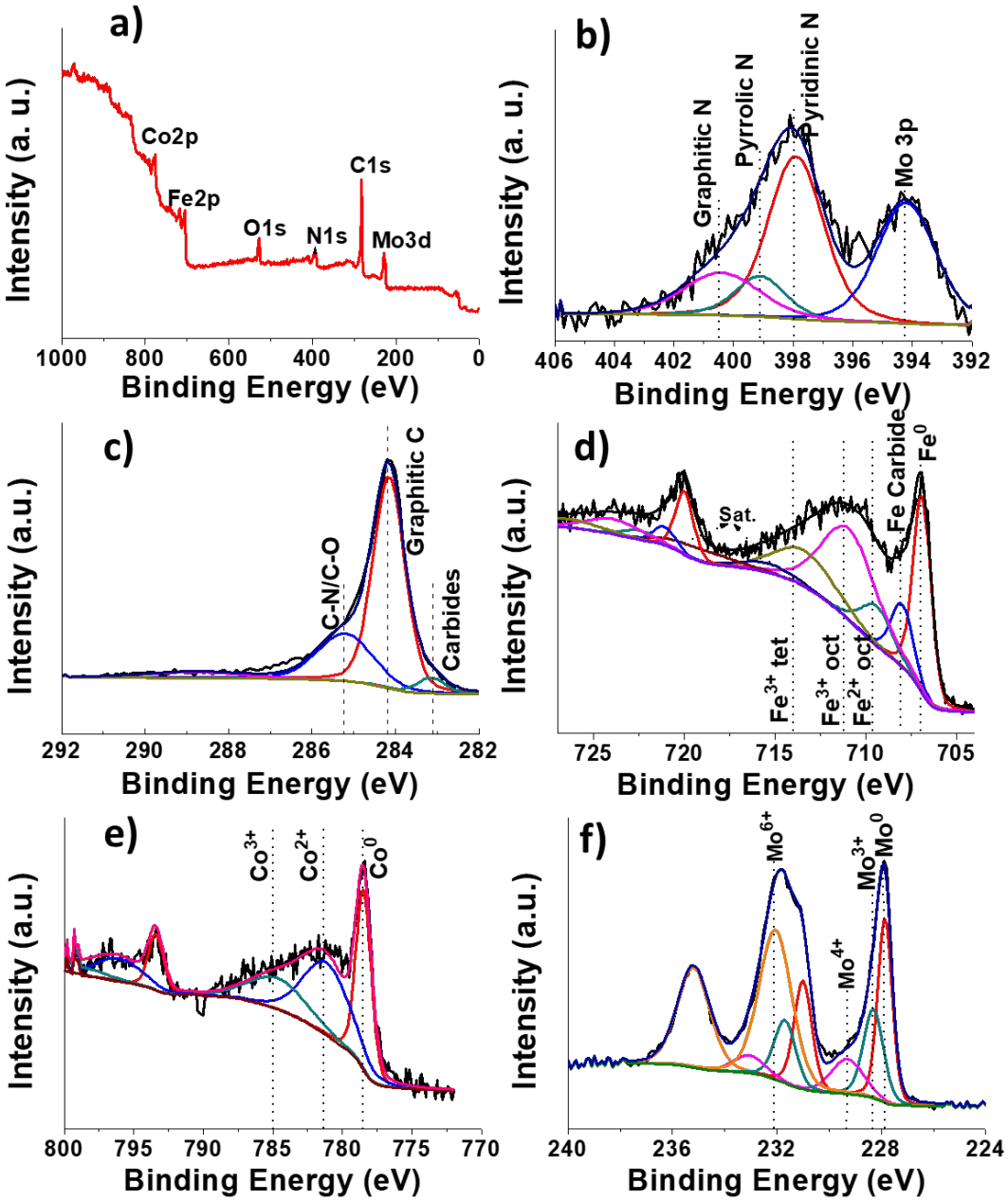

Figure 3. a) Overall XPS spectrum of Mo_2C-NC@CoFe (sample 5) as-formed upon pyrolysis of the corresponding precursor at 600 °C, and the related high-resolution XPS spectra of b) N1s, c) C1s, d) Fe2p, e) Co2p and f) Mo3d.

High-resolution XPS spectra revealed a detailed surface composition of the Mo_2C-NC@CoFe composite material. Figure 3b shows that the nitrogen is mainly present as pyridinic (63.2%) and graphitic nitrogen (22.6%), whereas the amount of pyrrolic nitrogen is lower (14.3%). Due to the nitrogen lone pair electrons, the electronic structure of the N-doped graphene is expected to favor mass diffusion and adsorption of the electrolyte as reported

previously.[10b] The C 1s XPS spectrum (Figure 3c) proved that the surface carbon atoms mainly consist of graphitic carbon (65.1%) and C-O/C-N (25.1%). In addition, a small peak at 283.14 eV indicates the presence of small amount of carbide species (4.2%). This peak position is close to the values (283.1 eV, 283.2 eV, 283.3 eV) previously attributed to Mo carbides,[16] whereas it slightly differs from the values reported for Mo_2C foil (282.9 eV)[17] and Mo_2C powder (282.7 eV),[18] respectively, most likely caused by the presence of Mo_2C nanoparticles in the composite material rather than bulk molybdenum carbide. The dominant peak in the Fe 2p spectrum (2p5/2 band, Figure 3d) at 706.84 eV points to a zero-valent Fe (24.7%), whereas the peak at 707.90 eV (12.4%) points to Fe carbides.[19] Additional peaks in the 2p5/2 band at higher binding energies result from Fe^{2+} and Fe^{3+} species. Similarly, most of the surface Co atoms are present as Co^{2+} and Co^{3+} species as shown in Figure 3e. However, the peak at 778.40 eV (34.8 %) in the Co 2p XPS spectrum (Figure 3e) also points to the presence of metallic Co at the particle surface.[20] The Mo 3d spectrum (Figure 3f) shows four oxidation states of Mo (Mo^0, Mo^{3+}, Mo^{4+}, and Mo^{6+}). In accordance with the XRD results, the Mo^0 and Mo^{3+} peaks with a total percentage of 43.2% are related to the Mo-Mo and Mo-C bonds of the Mo carbides on the surface. On the other hand, peaks due to higher oxidation states (Mo^{4+} and Mo^{6+}) revealed the existence of surface molybdenum oxides (MoO_2 and MoO_3).[21] The formation of molybdenum carbide is expected to be advantageous for the electrocatalytic properties of these materials since Mo_2C is known to be an active component in the hydrogen evolution reaction (HER), whereas the presence of Mo oxides, which results from the oxidation of surface Mo carbides upon exposure to air, is known to be rather disadvantageous for the HER reaction.[13a, 22]

2.2. Electrocatalytic properties: The electrocatalytic performance (HER, OER) of the Mo_2C-NC@CoFe material (sample 5) was studied by recording polarization curves in a three-electrode system with a platinum sheet and Ag/AgCl treated with 3.5 M KCl as the control electrode and reference electrode, respectively, while a rotating glassy carbon disk electrode

with a loading amount of 0.28 mg cm^{-2} was used as the working electrode in Ar-purged 1 M KOH solution. The results were compared with commercial precious materials (Pt-C, RuO_2) as well as with samples 1-3 and sample 7, which contain different metal sources (Fe, Co, and Mo). As expected, the commercial Pt-C exhibits an excellent HER catalytic activity with a negligible overpotential of about 40 mV (Figure 4a). The CoFe-free MoO_2-NC material (sample 2) shows poor HER activity at 10 mA cm^{-2} with a high overpotential of 510 mV. Such observation is in accordance with previous reports which proved that Mo oxides are indeed disadvantageous for HER reaction.[13a, 17] In contrast, the Mo-free NC@CoFe material (sample 1) shows a much lower overpotential of 280 mV, indicating that the CoFe alloy nanoparticles favor the HER reaction. Incorporation of molybdenum in the composite materials (sample 3 Mo_xC-NC@Co; sample 5 Mo_2C-NC@CoFe; sample 7 Mo_2C-NC@Fe/Fe_3C) resulted in reduced overpotentials of 170 mV, 190 mV and 252 mV at 10 mA cm^{-2}, respectively, which are lower than the overpotential value measured for the Mo-free sample 1. These results clearly showcase the synergistic effects of Co, Fe and Mo on the HER catalytic activity of the resulting composite materials. Taking into account the effect of Mo, Co, Fe atoms on the HER reaction catalyzed by these materials, the TOF for H_2 production is calculated at the iR-corrected overpotential of 200 mV. The resulting TOFs obtained with Mo_xC-NC@Co (sample 3, 2.95×10^{-2} s^{-1}) and Mo_2C-NC@CoFe (sample 5, 1.62×10^{-2} s^{-1}) are obviously larger than those obtained for NC@CoFe (sample 1, 4.38×10^{-3} s^{-1}) and Mo_2C-NC@Fe/Fe_3C (sample 7, 4.32×10^{-3} s^{-1}), respectively, further underlying the synergistic effect of Mo_2C and Co/Fe to improve the intrinsic activity of this kind of material.

Furthermore, as shown in Figure 4b, the highest OER activity with an overpotential of as low as 320 mV at 10 mA cm^{-2} is observed for the Mo_2C-NC@CoFe material (sample 5), whereas NC@CoFe (sample 1, 390 mV), Mo_xC-NC@Co (sample 3, 365 mV), and even commercial RuO_2 (402 mV) have higher overpotentials. Therefore, the outstanding HER and

OER activities of the multimetallic Mo_2C-NC@CoFe material (sample 5) point to a synergistic effect between the CoFe cores and the Mo_2C nanoparticles in the graphene shell. Given that the OER overpotentials for the Co-free Mo_2C-NC@Fe/Fe_3C (sample 7, 470 mV) and CoFe-free MoO_2-NC (sample 2, 448 mV) are close to the overpotential value of the blank GC electrode (490 mV), we concluded that the OER active sites mainly originate from the Co components. In this case, the TOF for O_2 production is roughly derived from the Co atoms in the material, which is based on the current density at an iR-corrected overpotential of 360 mV. The TOF for O_2 production obtained for Mo_2C-NC@CoFe (sample 5, 8.18×10^{-2} s^{-1}) is obviously larger than the values of NC@CoFe (sample 1, 5.40×10^{-3} s^{-1}), Mo_xC-NC@Co (sample 3, 9.13×10^{-3} s^{-1}) and the precious RuO_2 (5.75×10^{-3} s^{-1}), proving that the OER reaction of Mo_2C-NC@CoFe is faster compared to the other materials. In addition, the HER reaction of the Mo_2C-NC@CoFe material, which generally occurs via a Volmer-Heryrovsky process, revealed a Tafel slope of 110 mV/decade (Figure 4c) that is lower than the values observed with the Co and Fe-free sample MoO_2-NC (164 mV/decade) and Mo-free sample NC@CoFe (155 mV/decade). On the other hand, the much lower Tafel slope of 48 mV/decade and larger exchange current density of 36.08 mA cm^{-2} for the OER over the Mo_2C-NC@CoFe material also indicate a favorable OER process (Figure 4d).

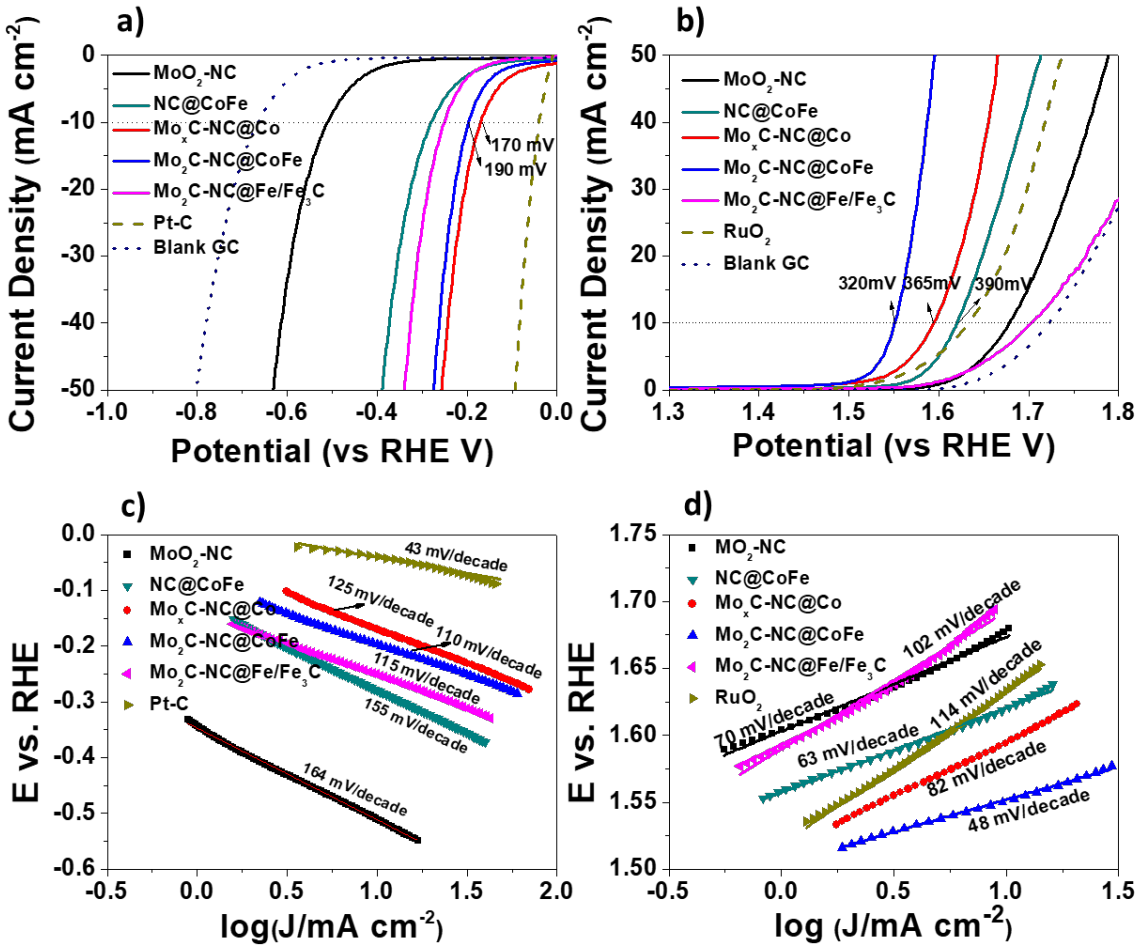

Figure 4. Electrochemical evaluations of different samples measured in 1 M KOH. a) The iR-corrected polarization curves for HER measured at a scan rate of 10 mV s^{-1}, b) The iR-corrected polarization curves for OER measured at a scan rate of 10 mV s^{-1}, c) The Tafel slopes for HER. d) The Tafel slopes for OER.

The polarization curves and chronoamperometry measurement of the Mo_2C-NC@CoFe material (sample 5) were further recorded by replacing the platinum sheet with a carbon paper as the control electrode. The resulting polarization curves agree well with the result based on the platinum sheet (Figures S6A, S6B), indicating that the catalytic activity for HER and OER is caused from the Mo_2C-NC@CoFe material rather than from possibly dissolved Pt from the control electrode. Furthermore, with the carbon paper as control electrode, the long-term stability of this material was studied, and more than 90% of the current observed for the Mo_2C-NC@CoFe material (sample 5) is preserved after performing HER or OER reactions for 10000 seconds (Figures S6C, S6D), which is much larger than the values obtained for Pt-

C (51%) and RuO_2 (39%), respectively. These results proved that the Mo_2C-NC@CoFe material is highly stable during the electrochemical measurement, which is further proved by XRD, EDX and TEM characterizations of sample 5 (Mo_2C-NC@CoFe) after the HER and OER treatment for 16 h (Figures S7-S12).

2.3. Role of Fe, Co and Mo sources on particle morphology, composition, and electrocatalytic properties: Besides introducing CoFe cores as active components for both HER and OER, we assume that the presence of Co and Fe promotes the formation of Mo_2C nanoparticles in the graphene shell, leading to the improvement of the HER activity of the composite materials. Based on the enhanced HER activities for sample 3 (Mo_xC-NC@Co) and sample 5 (Mo_2C-NC@CoFe) compared to sample 1 (NC@CoFe) and sample 2 (MoO_2-NC), the Mo carbides coupled in the graphene shell are favorable components for the HER process. The XRD pattern of the CoFe-free sample 2 (MoO_2-NC, Figure S13A), which was prepared from molybdic acid and melamine-formaldehyde resin without any Co and Fe sources, almost exclusively exhibits reflexes due to molybdenum oxide (MoO_2) rather than molybdenum carbide (Mo_2C). In contrast, the XRD patterns of sample 3 (Mo_xC-NC@Co), sample 5 (Mo_2C-NC@CoFe), and sample 7 (Mo_2C-NC@Fe/Fe_3C) (Figure S13A) revealed that the formation of MoO_2 is clearly hampered by the presence of Co or Fe sources. In addition, the XRD patterns of Fe-containing samples 5 and 7 showed the formation of crystalline Mo_2C nanoparticles. These findings are in accordance with previous reports, in which the presence of ferrite was found to have an advantageous effect on the formation of Mo_2C.[13b] In agreement with the results from XRD, the Mo 3d XPS spectrum (Figure S14C) of MoO_2-NC (sample 2) showed almost no peaks in the 3d5/2 band that are characteristic of the zero-valent Mo, which in contrast is clearly present for samples prepared in the presence of Co or Fe (Mo_xC-NC@Co, Mo_2C-NC@Fe and Mo_2C-NC@CoFe). These samples performed far better HER catalytic activity than the Mo-free sample 1 (NC@CoFe) and the CoFe-free sample 2 (MoO_2-NC).

The different electrocatalytic HER performances of the Mo-containing samples (Mo_xC-NC@Co, Mo_2C-NC@CoFe, and Mo_2C-NC@Fe/Fe_3C) with varying amounts of Co and Fe can be attributed to the variations of the location and particle size of Mo carbides in the composite materials. While the presence of crystalline molybdenum carbide phases in the Fe-free Mo_xC-NC@Co material (sample 3) could neither be proven by XRD (Figure S13A) nor by HR-TEM (Figures S15A1-A3), the half-substitution of Co by Fe in sample 5 (Mo_2C-NC@CoFe, Figures S15B1-B3) and Co-free sample 7 (Mo_2C-NC@Fe/Fe_3C, Figures S15C1-C3) resulted in the formation of crystalline Mo_2C domains in the graphene shell, whose mean size was found to increase from 6 nm (Mo_2C-NC@CoFe) to 15 nm (Mo_2C-NC@Fe/Fe_3C) with increasing amounts of Fe. Since larger Mo_2C nanoparticles tend to move to the graphene surface (Figures S15C1-C3) of the composite materials, the overall Mo surface concentration was shown to increase with increasing substitution rate (Table S4). However, the surface concentration of Mo oxides also increased due to an easier surface oxidation of the Mo_2C crystals on the graphene shell (Figure S14C, Table S6). Correspondingly, the overpotential for HER at 10 mA cm^{-2} increases with increasing Fe concentration as shown in Figure S16A. In addition, electrochemical impedance spectroscopy (EIS) of these materials was recorded to investigate the HER kinetics, and the Nyquist plots in Figure S16C clearly showed that the semicircle radius becomes larger with increasing Fe concentration, which indicates lower charge transfer resistance and more efficient charge transport during the HER reaction over these samples with lower Fe amount. Therefore, a low substitution rate of Co by Fe is beneficial for the formation of tiny Mo carbides embedded in the graphene shell, which ultimately favors the HER reaction.

As previously reported, experimental findings point to a stronger reactivity of Fe atoms with the carbon atoms from the surface graphene.[6g] Crystalline iron carbide (Fe_3C) was only formed in the Co-free sample 4 (Mo_2C-NC@Fe/Fe_3C, Figure S13C), whereas the formation of Co/Fe carbides in the Co-containing samples (Mo_2C-NC@CoFe, Mo_xC-NC@Co) was not

observed in the XRD patterns (Figure S13A). In addition, Raman spectroscopic studies showed an increase of the I_D/I_G value with increasing amount of Fe (Figure S17), which points to an increasing disorder of the graphene shell. Accordingly, the area of the quadrangle-shaped CV graph in the range of 0.16 to 0.36 V without apparent Faradaic process increases with increasing amount of Fe in sample 3-7 (Figure S16E), revealing a larger double-layer capacitance. This was further verified by a linear fitting of the current density at a constant potential of 0.25 V to the scan rates (20-140 mV s^{-1}) as shown in Figure S16F. Derived from these values, the electrochemical surface area (ESCA) of sample 3-7 were calculated to be 6.5 m^2 g^{-1} (3), 9.2 m^2 g^{-1}(4), 13.4 m^2 g^{-1}(5), 18.6 m^2 g^{-1} (6), and 24.6 m^2 g^{-1}(7), respectively. These findings indicate that the ESCA increases with increasing amount of Fe. Meanwhile, sample 4 (Fe:Co ratio roughly 1:2), which contained a slightly higher surface Co concentration (2.55 at%), displayed a better OER activity (334 mV, 10 mA cm^{-2}) than the Fe-free sample 3 (Mo_xC-NC@Co, 2.00 at%, 365 mV, 10 mA cm^{-2}) (Figure S16B), and it also generated a lower charge transfer resistance for OER process as revealed by the smaller semicircle radius in the Nyquist plots of Figure S16D. On the other hand, a positive shift in the binding energy for Co^0 is observed from the half-substitution of Co by Fe in sample 5 (Figure S14F). As a result, the OER activity is improved as can be seen by comparing sample 5 (320 mV, 10 mA cm^{-2}) with samples 3 and 4, even though the surface Co concentration of sample 5 (1.75 at% Co) is still lower than sample 3 (2.00 at%) and sample 4 (2.55 at%).

The disorder of the graphene shell not only relies on the presence of iron in the precursor material but also on the formation of Mo_2C nanoparticles. In contrast to the graphene layer of the Mo-free sample 1 (NC@CoFe, Figures S18A1-A3), the graphene layers adjacent to the Mo_2C nanocrystal for sample 5 (Mo_2C-NC@CoFe, Figures S18B1-B3) are partly damaged. In accordance with these findings, the Raman spectrum of sample 5 shows a slightly larger I_D/I_G value compared to that of sample 1 (Figure S19). At the same time, the presence of molybdenum influences the size of the CoFe core as can be seen when comparing the TEM

images of samples 5 and 1 (Figure S20). The presence of the Mo source (molybdic acid) in sample 5 seems to have a favorable effect on the thermal stability of the organic shell, hence resulting in the formation of smaller particles (Figures S21, S22). As a result, the Co surface concentration in sample 5 (Mo_2C-NC@CoFe, 1.75 at%) is higher than the corresponding concentration in sample 1 (NC@CoFe, 1.37 at%), whereas the bulk concentrations of Co and Fe are almost identical in both samples (Tables S2, S4). Accordingly, the OER overpotential of sample 5 (320 mV) is lower compared to sample 1 (390 mV). These findings further indicate a synergistic effect of iron and molybdenum on the structural disorder of the graphene shell as well as on the accessibility of Co, which overall enhances the OER activity of the Mo_2C-NC@CoFe material.

While the Mo_2C nanoparticles are required for the HER, Co is the active component for the OER. Consequently, the best electrocatalytic performance was observed for sample 5 (Mo_2C-NC@CoFe) containing all three metals. Since the electron transport among different active components is also expected to have a strong influence on the catalytic performance of the composite materials,[12b, 12c] further investigations are necessary. Based on our results, a precise control over the different metal components (Table S1, samples 3-9) can be used to tune the catalytic performance of the Mo_2C-NC@CoFe materials for HER and OER (Figures S16, S23). For instance, a further increase of the Co and Fe amounts in sample 9 (Mo_2C-NC@CoFe) resulted in a slightly lower OER overpotential (310 mV vs. 320 mV at 10 mA cm^{-2}), most likely due to the higher Co surface concentration when compared with sample 5 (Figure S23B, Table S4). Furthermore, an increase of the loading amounts on the GC electrode resulted in the lowest HER overpotential of 145 mV and an OER overpotential of 300 mV at 10 mV cm^{-2} (Figures S23E, S23F). Comparing our findings with previously reported materials based on Mo carbides coupled to 3d-TMs, the Mo_2C-NC@CoFe catalysts belong to one of the most efficient electrocatalysts for both HER and OER (Table S7).

2.4. Electrocatalytic performance of overall water splitting reaction: Sample 9 (Mo_2C-NC@CoFe) was evaluated as bi-functional electrocatalysts loaded on Ni foams for overall water splitting in 1 M KOH electrolyte. The potentials of the cell built with Mo_2C-NC@CoFe on the cathode and anode sides could be further reduced by increasing the sample loading amount (Figure 5a). The lowest potential of 1.53 V (onset potential 1.42 V) at a current density of 10 mA cm^{-2} was observed with a catalyst loading of 5 mg cm^{-2} (Figure 5b), which is about 70 mV lower than the values obtained with the same amount of Pt-C and RuO_2 respectively supported on a cathode and an anode. Moreover, water splitting can also proceed at 1.6 V at 20 mA cm^{-2}, which is almost 30 mV lower than the potentials of the cell composed of Pt-C and RuO_2 catalysts. In addition, an even lower potential of 1.43 V at a current density of 10 mA cm^{-2} was obtained with a cell containing the Fe-free sample Mo_xC-NC@Co on the cathode and Mo_2C-NC@CoFe (sample 9) on the anode side. The Faraday efficiencies of 92 % (oxygen production) and 96% (hydrogen production) were obtained by using the Mo_2C-NC@CoFe material as both cathode and anode catalysts in a two-electrode system. Furthermore, the Mo_2C-NC@CoFe catalyst showed a long-term stability upon water splitting reactions at a constant potential of 10 mA cm^{-2} for 16 h, which is better than the precious catalysts (Figures 5c, 5d). The electrocatalytic activity of the as-prepared Mo_2C-NC@CoFe material for overall water splitting is even better than recently reported Ni_3S_2 NWs/Ni (1.63 V, 10 mA cm^{-2}),[23] Co1Mn1CH/NF (1.63 V, 10 mA cm^{-2}),[24] CoP/TM (1.64 V, 10 mA cm^{-2})[25] and Ni_5P_4/NF (1.69V, 10 mA cm^{-2}),[2a] respectively. Mo_2C-NC@3d-TMs materials are therefore proven to be one of the most efficient non-precious electrocatalysts for the overall water splitting in basic electrolyte (Table S8).

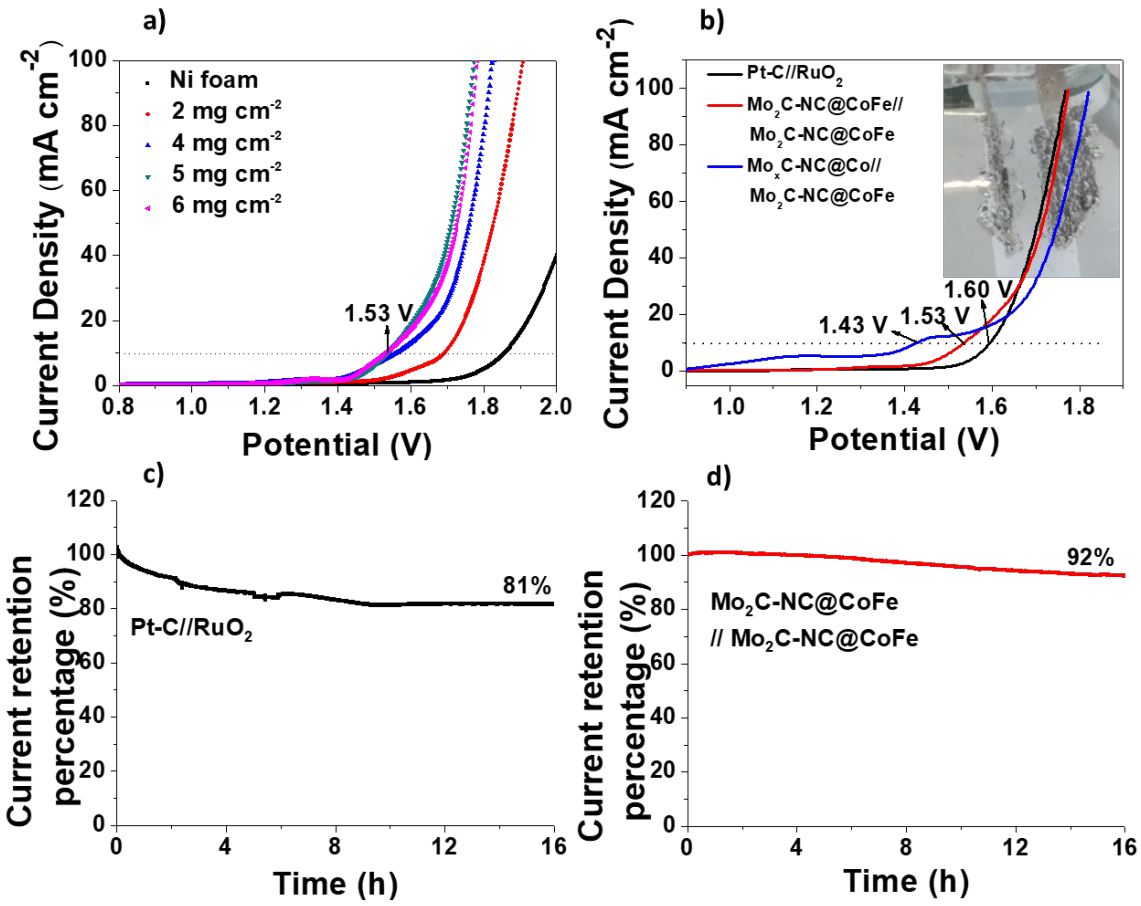

Figure 5. a) The electrochemical performance of the overall water splitting over the Mo_2C-NC@CoFe material of sample 9 at various loading amount on nickel foam in 1 M KOH. b) The iR-corrected polarization curves for the overall water splitting measured at a scan rate of 10 mV s^{-1} with a loading amount of 5 mg cm^{-2} on the nickel foams, inset is the photo of home-made cell composed by the Mo_2C-NC@CoFe material of sample 9 with obvious bubbles on the electrode surface at 10 mA cm^{-2}. c) The current retention during overall water splitting over commercial precious catalysts at a constant voltage. d) The current retention during overall water splitting over the Mo_2C-NC@CoFe material of sample 9 at a constant voltage.

2.5. Electrocatalytic performance in acidic media: The performance of these electrocatalysts in acidic media (0.5 M H_2SO_4) was further investigated with a carbon paper as the control electrode as shown in Figure S24. It was revealed that the Mo_2C-NC@CoFe material (sample 5) has a lower overpotential (-240 mV) and Tafel slope (67 mV/decade) than other materials except for Pt-C (Figures S24 A, S24B), indicating better electrochemical activity for HER in acidic media. The smaller radius of the semicircle in the Nyquist plot (Figure S24 C) furthermore proved that the charge transport obtained for the Mo_2C-

NC@CoFe material (sample 5) is more efficient compared to other materials. Moreover, the larger area of the rectangular-shaped CV graph (Figure S24D) clearly revealed that this material has a larger double-layer capacitance, which is also favorable for the mass adsorption and charge transport. Even though the activity of the Mo_2C-NC@CoFe material is lower compared with Pt-C as shown by the polarization curve and Tafel slope, the far higher long-term stability of the Mo_2C-NC@CoFe material (Figure S24E) compared with the precious Pt-C in 0.5 M H_2SO_4 renders this material very promising for technical applications.

3. Conclusion

Mo_2C-NC@CoFe composite materials were synthesized by controlled calcination of cobalt ferrite spinel nanoparticles coated by a molybdic acid-cross linked MF resin. The coalescence of the active components was inhibited during the calcination process. The Co and Fe sources were found to promote the formation of Mo carbides, which are the HER active sites. Moreover, the favorable effect of the Fe and Mo sources on the OER is related to a "disordering effect" on the graphene layer caused by the formation of molybdenum and iron carbides, which results in an enhanced surface Co accessibility. Synergistically, the Mo_2C-NC@CoFe composite materials show very promising potential as highly active bi-functional electrocatalysts for overall water splitting. Potential as low as 1.53 V at a current density of 10 mA cm^{-2} were reached in basic electrolyte, which is more efficient than the overall water splitting catalyzed by commercial precious catalysts. Hence, this work opens a new avenue to introduce TMs-based materials as multi-functional catalysts.

4. Experimental Section

Preparation of Mo_2C-NC@CoFe materials: Monodispersed Co-substituted Fe_3O_4 spinel nanoparticles prepared by solvothermal methods were used as metal sources (E1 in the supporting information).[26] Typically, spinel nanoparticles prepared with 1.5 mmol Co and

1.5 mmol Fe precursor were dispersed in 18 mL of ethanol and 2 mL of deionized water followed by the addition of 0.5 mmol molybdenum acid and 1.5 molar citrate acid. which improved the solubility of molybdic acid.[27] Thereafter, 1.5 mmol melamine and 0.6 mL formaldehyde were added to the stirred solution, which was then heated at 136 °C for 16 h in an autoclave reactor. The resulting spinel NPs coated by melamine-formaldehyde (MF) resins cross-linked with molybdic acid were isolated by centrifugation and dried in oven at 120 °C. Annealing these particles in an Ar flow at 600 °C yielded the desired Mo_2C embedded in N-doped graphene encapsulating CoFe alloy materials (Mo_2C-NC@CoF*e*). Detailed preparation parameters for other samples are presented in Table S1.

Characterizations: Transmission electron microscope (TEM) and EDX elemental maps were recorded on a JEM-2200FS Microscope. X-ray diffraction patterns were collected on a Bruker D8 Advance Discover X-ray Diffractometer with a Cu Ka radiation. The surface contents and species were analyzed by the X-ray photoelectron spectroscopy on a PHI VersaProbe II Scanning XPS Microprobe, and all of the spectra are calibrated to the adventitious carbon 1s peak at 284.8 eV. The elemental content of Co and Fe in the products were determined by atomic absorption spectroscopy on SOLAAR M Series AA Spectrometer, and the samples were pre-dissolved in concentrated nitric acid under heating conditions and diluted to a constant volume. The amount of Mo in the materials was determined by UV/vis spectroscopy using a Varian Cary 300 UV-Vis (details are given in the supporting information), whereas the other elements were quantified by use of an EURO EA Elemental Analyzer. Fourier-transformed infrared spectra (FTIR) were recorded on a Bruker ATR Spectrometer, and the graphitic structure was analyzed by Raman spectroscopy with a Renishaw InVia Raman Microscope.

Electrochemical evaluation: The electrochemical performance of the catalysts was evaluated by a common three-electrode system using a suitable instrument from Metrohm Autolab with Nova software. Platinum sheets with a surface area of 1 cm^2 were used as the control

electrode. Ag/AgCl treated with 3.5 M KCl solution was employed as the reference electrode. The working electrode was prepared with 3 mg catalyst materials, which was added to a mixture of 50 μL 95% Nafion solution, 250 μL ethanol, and 250 μL pure water and treated by sonication for 30 min. Typically, 10 μL of the obtained ink was dropped onto the surface of a rotating disc GC electrode and dried in an oven at 60 °C, resulting in a loading amount of 0.28 mg cm^{-2}. The performances of as-prepared electrodes were evaluated mainly in 1 M KOH electrolyte and compared with the commercial catalysts Pt-C and RuO_2. Linear scan curves were recorded at a scan rate of 10 mV s^{-1} with a rotating speed of 1600 rpm to analyze the activity for catalyzing the hydrogen evolution reaction (HER) and the oxygen evolution reaction (OER), which were iR-corrected directly on the instrument. Electrochemical impedance spectroscopies were tested to characterize the properties of mass and charge transport, while cyclic voltammogram graphs were obtained at different scan rate (20-140 mV s^{-1}) to calculate the electrochemical surface area (ESCA). The potentials applied were transformed into the value referred to the reversible hydrogen electrode (RHE) by the following equation: E (vs RHE) = E (Ag/AgCl) + 0.204+ 0.0592*pH.

The overall water splitting was tested in a home-made two-electrode cell. Different amounts of catalyst materials were loaded onto a Nickel foam of 1 cm^2. Before that, 5 mg of the prepared materials were dispersed into PTFE ethanol and water solution by sonication for 30 min, and the ink was dropped onto the Nickel foam slowly. After drying, they were employed as electrodes for both HER and OER. For comparison, Pt-C and RuO_2 were used as cathode and anode materials for water splitting. Linear scan curves and the time dependence of current density were recorded to respectively analyze the activity and stability of these materials. Besides, the calculation methods for electrochemical surface area (ESCA) turnover frequency (TOF) and Faradaic efficient (FE) are illustrated in the supporting information.

Supporting Information

Supporting Information is available from the Wiley Online Library or from the author.

Acknowledgements
This work was supported by the Deutsche Forschungsgemeinschaft (DFG) within the CRC/TRR 247 "Heterogeneous Oxidation Catalysis in the Liquid Phase" (project C03), the DFG core facility "Interdisciplinary Center for Analytics on the Nanoscale" (ICAN) at the Center for Nanointegration Duisburg-Essen (CENIDE) and the University of Duisburg-Essen. S. P. Wang is thankful to the Humboldt Foundation for a Postdoctoral Research Fellowship. We thank Dr. M. Heidelmann and Dr. U. Hagemann for analytical support (TEM, XPS).

Received: ((will be filled in by the editorial staff))
Revised: ((will be filled in by the editorial staff))
Published online: ((will be filled in by the editorial staff))

References

[1] a) J. A. Turner, *Science* **1999**, *285*, 687; b) F. Cheng, J. Chen, *Chem. Soc. Rev.* **2012**, *41*, 2172; c) L. Schlapbach, *Nature* **2009**, *460*, 809.
[2] a) M. Ledendecker, S. Krick Calderon, C. Papp, H. P. Steinruck, M. Antonietti, M. Shalom, *Angew. Chem. Int. Ed.* **2015**, *54*, 12361; b) Q. Xiong, Y. Wang, P. F. Liu, L. R. Zheng, G. Wang, H. G. Yang, P. K. Wong, H. Zhang, H. Zhao, *Adv. Mater.* **2018**, *30*, 1801450; c) V. Raghuveer, A. Manthiram, A. J. Bard, *J. Phys. Chem. B* **2005**, *109*, 22909; d) K. Fugane, T. Mori, D. R. Ou, P. Yan, F. Ye, H. Yoshikawa, J. Drennan, *Langmuir* **2012**, *28*, 16692; e) A. Jackson, A. Strickler, D. Higgins, T. F. Jaramillo, *Nanomaterials* **2018**, *8*, 38; f) G. Zhao, K. Rui, S. Dou, and W. Sun, *Adv. Funct. Mater.* **2018**, *28*, 1803291.
[3] a) B. Y. Xia, Y. Yan, N. Li, H. B. Wu, X. W. Lou, X. Wang, *Nat. Energy* **2016**, *1*, 15006; b) P. Chen, T. Zhou, L. Xing, K. Xu, Y. Tong, H. Xie, L. Zhang, W. Yan, W. Chu, C. Wu, Y. Xie, *Angew. Chem. Int. Ed.* **2017**, *56*, 610; c) M. K. Debe, *Nature* **2012**, *486*, 43.
[4] a) X. Kong, K. Xu, C. Zhang, J. Dai, S. Norooz Oliaee, L. Li, X. Zeng, C. Wu, Z. Peng, *ACS Catal.* **2016**, *6*, 1487; b) Y. C. Lu, Z. Xu, H. A. Gasteiger, S. Chen, K. Hamad-Schifferli, Y. Shao-Horn, *J. Am. Chem. Soc.* **2010**, *132*, 12170; c) S. Drouet, J. Creus, V. Colliere, C. Amiens, J. Garcia-Anton, X. Sala, K. Philippot, *Chem. Commun.* **2017**, *53*, 11713; d) J. Mahmood, F. Li, S. M. Jung, M. S. Okyay, I. Ahmad, S. J. Kim, N. Park, H. Y. Jeong, J. B. Baek, *Nat. Nanotech.* **2017**, *12*, 441; e) C. Massue, X. Huang, A. Tarasov, C. Ranjan, S. Cap, R. Schlogl, *ChemSusChem* **2017**, *10*, 1958.
[5] a) D. Escalera-Lopez, Y. Niu, J. Yin, K. Cooke, N. V. Rees, R. E. Palmer, *ACS Catal.* **2016**, *6*, 6008; b) P. D. Tran, T. V. Tran, M. Orio, S. Torelli, Q. D. Truong, K. Nayuki, Y. Sasaki, S. Y. Chiam, R. Yi, I. Honma, J. Barber, V. Artero, *Nat. Mater.* **2016**, *15*, 640; c) B. Cao, G. M. Veith, J. C. Neuefeind, R. R. Adzic, P. G. Khalifah, *J. Am. Chem. Soc.* **2013**, *135*, 19186; d) K. Xu, P. Chen, X. Li, Y. Tong, H. Ding, X. Wu, W. Chu, Z. Peng, C. Wu, Y. Xie, *J. Am. Chem. Soc.* **2015**, *137*, 4119; e) X. Xu, Y. Chen, W. Zhou, Z. Zhu, C. Su, M. Liu, Z. Shao, *Adv. Mater.* **2016**, *28*, 6442; f) Y. Zhu, W. Zhou, Z. G. Chen, Y. Chen, C. Su, M. O. Tade, Z. Shao, *Angew. Chem. Int. Ed.* **2015**, *54*, 3897; g) C. Hu, L. Zhang, Z. J. Zhao, J. Luo, J. Shi, Z. Huang, J. Gong, *Adv. Mater.* **2017**, *29, 1701820*; h) R. Subbaraman, D. Tripkovic, K. C. Chang, D. Strmcnik, A. P. Paulikas, P. Hirunsit, M. Chan, J. Greeley, V. Stamenkovic, N. M. Markovic, *Nat. Mater.* **2012**, *11*, 550; i) H. Fei, J. Dong, Y. Feng, C. S. Allen, C. Wan, B. Volosskiy, M. Li, Z. Zhao, Y. Wang, H. Sun, P. An, W. Chen, Z. Guo, C. Lee, D. Chen, I. Shakir, M. Liu, T. Hu, Y. Li, A. I. Kirkland, X. Duan, Y. Huang, *Nat. Catal.* **2018**, *1*, 63.
[6] a) Y. Fan, S. Ida, A. Staykov, T. Akbay, H. Hagiwara, J. Matsuda, K. Kaneko, T. Ishihara, *Small* **2017**, *13, 1700099*; b) P. Chen, K. Xu, Z. Fang, Y. Tong, J. Wu, X. Lu, X. Peng, H. Ding, C. Wu, Y. Xie, *Angew. Chem. Int. Ed.* **2015**, *54*, 14710; c) X. Fan, Z. Peng, R. Ye, H. Zhou, X. Guo, *ACS nano* **2015**, *9*, 7407; d) S. Cobo, J. Heidkamp, P. A. Jacques, J. Fize, V. Fourmond, L. Guetaz, B. Jousselme, V. Ivanova, H. Dau, S. Palacin, M. Fontecave, V. Artero, *Nat. Mater.* **2012**, *11*, 802; e) L. Trotochaud, S. L. Young, J. K. Ranney, S. W.

Boettcher, *J. Am. Chem. Soc.* **2014**, *136*, 6744; f) S. E. Fosdick, S. P. Berglund, C. B. Mullins, R. M. Crooks, *ACS Catal.* **2014**, *4*, 1332; g) M.-Q. Wang, C. Ye, M. Wang, T.-H. Li, Y.-N. Yu, S.-J. Bao, *Energy Storage Mater.* **2018**, *11*, 112.
[7] a) Y. Tong, P. Chen, T. Zhou, K. Xu, W. Chu, C. Wu, Y. Xie, *Angew. Chem. Int. Ed.* **2017**, *56*, 7121; b) H. Jin, J. Wang, D. Su, Z. Wei, Z. Pang, Y. Wang, *J. Am. Chem. Soc.* **2015**, *137*, 2688; c) Y. Jiao, Y. Zheng, M. Jaroniec, S. Z. Qiao, *Chem. Soc. Rev.* **2015**, *44*, 2060.
[8] a) M. S. Burke, L. J. Enman, A. S. Batchellor, S. Zou, S. W. Boettcher, *Chem. Mater.* **2015**, *27*, 7549; b) R. L. Doyle, I. J. Godwin, M. P. Brandon, M. E. Lyons, *Phys. Chem. Chem. Phys.* **2013**, *15*, 13737; c) M. Bajdich, M. Garcia-Mota, A. Vojvodic, J. K. Norskov, A. T. Bell, *J. Am. Chem. Soc.* **2013**, *135*, 13521.
[9] a)Y. Liang, Y. Li, H. Wang, J. Zhou, J. Wang, T. Regier, H. Dai, *Nat. Mater.* **2011**, *10*, 780; b) X. Yan, Y. Jia, J. Chen, Z. Zhu, X. Yao, *Adv. Mater.* **2016**, *28*, 8771; c) Y. Liang, H. Wang, P. Diao, W. Chang, G. Hong, Y. Li, M. Gong, L. Xie, J. Zhou, J. Wang, T. Z. Regier, F. Wei, H. Dai, *J. Am. Chem. Soc.* **2012**, *134*, 15849.
[10] a) J. Du, C. Chen, F. Cheng, J. Chen, *Inorg. Chem.* **2015**, *54*, 5467; b) X. Zou, X. Huang, A. Goswami, R. Silva, B. R. Sathe, E. Mikmekova, T. Asefa, *Angew. Chem. Int. Ed.* **2014**, *53*, 4372; c) C. Lu, D. Tranca, J. Zhang, F. N. Rodri Guez Hernandez, Y. Su, X. Zhuang, F. Zhang, G. Seifert, X. Feng, *ACS nano* **2017**, *11*, 3933.
[11] a) G. Nam, J. Park, M. Choi, P. Oh, S. Park, M. G. Kim, N. Park, J. Cho, J. S. Lee, *ACS nano* **2015**, *9*, 6493; b) J. Deng, P. Ren, D. Deng, X. Bao, *Angew. Chem. Int. Ed.* **2015**, *54*, 2100; c) M. Tavakkoli, T. Kallio, O. Reynaud, A. G. Nasibulin, C. Johans, J. Sainio, H. Jiang, E. I. Kauppinen, K. Laasonen, *Angew. Chem. Int. Ed.* **2015**, *54*, 4535; d) T. Li, Y. Lu, S. Zhao, Z.-D. Gao, Y.-Y. Song, *J. Mater. Chem. A* **2018**, *6*, 3730.
[12] a) S. Wang, J. Wang, M. Zhu, X. Bao, B. Xiao, D. Su, H. Li, Y. Wang, *J. Am. Chem. Soc.* **2015**, *137*, 15753; b) M. Kim, S. Kim, D. Song, S. Oh, K. J. Chang, E. Cho, *Appl. Catal. B: Environ.* **2018**, *227*, 340; c) X. Xu, F. Nosheen, X. Wang, *Chem. Mater.* **2016**, *28*, 6313; d) Z. Y. Yu, Y. Duan, M. R. Gao, C. C. Lang, Y. R. Zheng, S. H. Yu, *Chem. Sci.* **2017**, *8*, 968; e) J. Jiang, Q. Liu, C. Zeng, L. Ai, *J. Mater. Chem. A* **2017**, *5*, 16929; f) X. Zhang, L. Huang, Y. Han, M. Xu, S. Dong, *Nanoscale* **2017**, *9*, 5583; g) F. Yu, Y. Gao, Z. Lang, Y. Ma, L. Yin, J. Du, H. Tan, Y. Wang, Y. Li, *Nanoscale* **2018**, *10*, 6080.
[13] a) H. Vrubel, X. Hu, *Angew. Chem. Int. Ed.* **2012**, *51*, 12703; b) C. Wan, Y. N. Regmi, B. M. Leonard, *Angew. Chem. Int. Ed.* **2014**, *53*, 6407; c) R. Ma, Y. Zhou, Y. Chen, P. Li, Q. Liu, J. Wang, *Angew. Chem. Int. Ed.* **2015**, *54*, 14723; d) F. Li, X. Zhao, J. Mahmood, M. S. Okyay, S. M. Jung, I. Ahmad, S. J. Kim, G. F. Han, N. Park, J. B. Baek, *ACS nano* **2017**, *11*, 7527; e) J. S. Li, Y. Wang, C. H. Liu, S. L. Li, Y. G. Wang, L. Z. Dong, Z. H. Dai, Y. F. Li, Y. Q. Lan, *Nat. Commun.* **2016**, *7*, 11204; f) M. Miao, J. Pan, T. He, Y. Yan, B. Y. Xia, X. Wang, *Chemistry* **2017**, *23*, 10947.
[14] X. Liu, M. Antonietti, *Adv. Mater.* **2013**, *25*, 6284.
[15] a) J.-S. Li, Y.-J. Tang, C.-H. Liu, S.-L. Li, R.-H. Li, L.-Z. Dong, Z.-H. Dai, J.-C. Bao, Y.-Q. Lan, *J. Mater. Chem. A* **2016**, *4*, 1202; b) M. Gong, Y. Li, H. Wang, Y. Liang, J. Z. Wu, J. Zhou, J. Wang, T. Regier, F. Wei, H. Dai, *J. Am. Chem. Soc.* **2013**, *135*, 8452; c) X. Fan, Y. Liu, S. Chen, J. Shi, J. Wang, A. Fan, W. Zan, S. Li, W. A. Goddard 3rd, X. M. Zhang, *Nat. Commun.* **2018**, *9*, 1809; d) D. Friebel, M. W. Louie, M. Bajdich, K. E. Sanwald, Y. Cai, A. M. Wise, M. J. Cheng, D. Sokaras, T. C. Weng, R. Alonso-Mori, R. C. Davis, J. R. Bargar, J. K. Norskov, A. Nilsson, A. T. Bell, *J. Am. Chem. Soc.* **2015**, *137*, 1305.
[16] a) F. Solymosi, J. Cserényi, A. Szöke, T. Bánsági, A. Oszkó, *J. Catal.* **1997**, *165*, 150; b) M. J. Ledoux, C. P. Huu, J. Guille, H. Dunlop, *J. Catal.* **1992**, *134,* 383; c) T. P. St. Clair, S. T. Oyama, D. F. Cox, S. Otani, Y. Ishizuka, R.-L. Lo, K. Fukui, Y. Iwasawa, *Surf. Sci.* **1999**, 426, 187.
[17] J. Wang, M. Castonguay, J. Deng, P. H. McBreen, *Surface Science* **1997**, *374*, 197.

[18] K. Hamrin, G. Johansson, A. Fahlman, C. Nordling, *J. Phys. Chem. Solids* **1969**, *30*, 1835.
[19] P. Tan, *J. Catal.* **2016**, *338*, 21.
[20] Z. H. Xue, H. Su, Q. Y. Yu, B. Zhang, H. H. Wang, X. H. Li, J. S. Chen, *Adv. Energy Mater.* **2017**, *7*, 1602355.
[21] K. Oshikawa, M. Nagai, S. Omi, *J. Phys. Chem. B* **2001**, *105*, 9124.
[22] M. Xiang, D. Li, W. Li, B. Zhong, Y. Sun, *Catal. Commun.* **2007**, *8*, 513.
[23] D. Zhang, J. Li, J. Luo, P. Xu, L. Wei, D. Zhou, W. Xu, D. Yuan, *Nanotechnology* **2018**, *29*, 245402.
[24] T. Tang, W. J. Jiang, S. Niu, N. Liu, H. Luo, Y. Y. Chen, S. F. Jin, F. Gao, L. J. Wan, J. S. Hu, *J. Am. Chem. Soc.* **2017**, *139*, 8320.
[25] L. Yang, H. Qi, C. Zhang, X. Sun, *Nanotechnology* **2016**, *27*, 23LT01.
[26] a) K. Chakrapani, G. Bendt, H. Hajiyani, T. Lunkenbein, M. T. Greiner, L. Masliuk, S. Salamon, J. Landers, R. Schlögl, H. Wende, R. Pentcheva, S. Schulz, M. Behrens, *ACS Catalysis* **2018**, *8*, 1259; b) K. Chakrapani, G. Bendt, H. Hajiyani, I. Schwarzrock, T. Lunkenbein, S. Salamon, J. Landers, H. Wende, R. Schlögl, R. Pentcheva, M. Behrens, S. Schulz, *Chem. Cat. Chem*. **2017**, *9*, 2988.
[27] T. E. Klimova, D. Valencia, J. Arturo Mendoza-Nieto, P. Hernández-Hipólito, *J. Catal.* **2013**, *304*, 29.

DOI: 10.1002/ente.201801121
URN: urn:nbn:de:hbz:464-20210127-141431-4

This is the peer reviewed version of the following article: Wang, S., Bendt, G., Saddeler, S., Schulz, S.: Synergistic Effects of Mo2C-NC@CoxFey Core–Shell Nanoparticles in Electrocatalytic Overall Water Splitting Reaction. *Energy Technol.* 2019, 7, 1801121, which has been published in final form at: https://doi.org/10.1002/ente.201801121